doi:10.1088/0004-637X/735/2/83

MODELING THE MODULATION OF GALACTIC AND JOVIAN ELECTRONS BY STOCHASTIC PROCESSES

R. D. Strauss[1], M. S. Potgieter[1], I. Büsching[1,2], and A. Kopp[1,3]
[1] Centre for Space Research, North-West University, Potchefstroom, 2520, South Africa; dutoit.strauss@nwu.ac.za
[2] Institut für Theoretische Physik, Lehrstuhl IV: Weltraum- und Astrophysik, Ruhr-Universität Bochum, 44780 Bochum, Germany
[3] Institut für Experimentelle und Angewandte Physik, Christian-Albrechts-Universität zu Kiel, Leibnizstraße 11, 24118 Kiel, Germany
Received 2010 December 15; accepted 2011 April 20; published 2011 June 20

ABSTRACT

We present a newly developed numerical modulation model to study the transport of galactic and Jovian electrons in the heliosphere. The model employs stochastic differential equations (SDEs) to solve the corresponding transport equation in five dimensions (time, energy, and three spatial dimensions) which is difficult to accomplish with the numerical schemes used in finite difference models. Modeled energy spectra for galactic electrons are compared for the two drift cycles to observations at Earth. Energy spectra and radial intensity profiles of galactic and Jovian electrons are compared successfully to results from previous studies. In line with general drift considerations, it is found that most 100 MeV electrons observed at Earth enter the heliosphere near the equatorial regions in the $A > 0$ cycle, while they enter mainly over the polar regions in the $A < 0$ cycle. Our results indicate that 100 MeV electrons observed at Earth originate at the heliopause with ~600 MeV undergoing adiabatic cooling during their transport to Earth. The mean propagation time of these particles varies between ~180 and 300 days, depending on the drift cycle. For 10 MeV Jovian electrons observed at Earth, a mean propagation time of ~40 days is obtained. During this time, the azimuthal position of the Jovian magnetosphere varies by ~1°. At a 50 AU observational point, the mean propagation time of these electrons increases to ~370 days with an azimuthal position change of Jupiter of ~20°. The SDE approach is very effective in calculating these propagation times.

Key words: cosmic rays – diffusion – methods: numerical – Sun: heliosphere

Online-only material: color figure

1. INTRODUCTION

Cosmic rays (CRs), as charged particles, propagating through the heliosphere are subjected to a variety of physical processes. These processes cause changes in CR intensities, referred to as CR modulation. The primary aim of CR modulation studies, and also the aim of this study, is to model this modulation as realistically as possible, thereby deepening our present understanding of the physical processes involved and how they affect CRs. To succeed in this purpose, it is necessary to compare computational results, at least qualitatively, to CR observations.

Due to the complexity of the transport equations (TPEs) applicable to CR modulation, these equations are typically solved numerically, often employing finite difference methods (e.g., Jokipii & Kopriva 1979). These methods have several disadvantages, most notoriously numerical instability problems when solving differential equations in higher dimensions. We present a newly developed CR modulation model that solves the relevant TPE by means of stochastic differential equations (SDEs). This method has several advantages, most notably unconditional numerical stability and independence of a spatial grid. Also, it will be shown that it is possible to extract additional physical insights from this method. SDEs were previously used to model the transport of pick-up ions in the heliosphere (Fichtner et al. 1996), CR acceleration in astrophysical systems (Krülls & Achterberg 1994), and CR transport (Yamada et al. 1999; Zhang 1999; Florinski & Pogorelov 2009; Pei et al. 2010). We follow Pei et al. (2010) and deviate from most previous works by solving the set of SDEs directly in spherical coordinates instead of Cartesian coordinates. The model is applied to the study of galactic and Jovian electrons, neither of which have been studied previously using SDE type models.

Galactic electrons are assumed to enter the heliosphere isotropically, with their intensities just outside the heliosphere specified by the local interstellar spectrum (LIS), whereafter they undergo modulation. The modulation of these electrons was studied previously by, e.g., Potgieter & Moraal (1985), Fichtner et al. (2000), and Potgieter & Langner (2004). In this paper, we aim to gain further insight into the modulation processes provided by the SDE approach. The same can be said for the study of Jovian electrons. The latter were discovered during the Pioneer 10 encounter of Jupiter, when it was realized that the Jovian magnetosphere is a very strong source of low energy (~10 MeV) electrons (e.g., Teegarden et al. 1974). Subsequent modeling of the Jovian electrons (e.g., Ferreira et al. 2001a) showed that these electrons are indeed the dominant CR electron component in the inner heliosphere at low energies. See also the reviews by Ferreira (2005), Heber & Potgieter (2006, 2008), and Heber et al. (2007).

2. THE MODULATION MODEL

For a nearly isotropic pitch-angle CR distribution function $f(r, \theta, \varphi, E, t)$, the transport of CRs inside the heliosphere can be described by the well-known Parker (1965) TPE,

$$\frac{\partial j}{\partial t} = -\left(V_{\rm sw} + \langle v_d \rangle\right) \cdot \nabla j + \nabla \cdot (\mathbf{K}_s \cdot \nabla j) + \frac{1}{3}\left(\nabla \cdot V_{\rm sw}\right)\frac{\partial}{\partial E}(\Gamma E j) + S, \quad (1)$$

which contains all the relevant transport processes inside the supersonic solar wind flow (i.e., inside the region between the Sun and the solar wind termination shock, TS). The differential intensity j is related to f by $j = P^2 f$, with P the particle rigidity. In the turbulent heliosheath region it has become custom to also consider second-order energy effects, e.g., momentum diffusion, which can readily be added to the existing TPE (e.g., Strauss et al. 2010).

In Equation (1), S describes a particle source term, e.g., Jupiter as the source of the Jovian electrons, V_{sw} is the solar wind flow which we take, for simplicity, to be directed radially outward $V_{sw} = V_{sw}\mathbf{e}_r$ with a constant speed of $V_{sw} = 400$ km s^{-1}, $\langle v_d \rangle$ is the pitch-angle averaged guiding center drift velocity, $\mathbf{K}_s$ is the symmetric diffusion tensor, given in heliospheric magnetic field (HMF) aligned coordinates by

$$\mathbf{K_s} \equiv \begin{matrix} \kappa_{||} & 0 & 0 \\ 0 & \kappa_{\perp\theta} & 0 \\ 0 & 0 & \kappa_{\perp r} \end{matrix}, \quad (2)$$

and $\nabla \cdot V_{sw}$ is the divergence of the solar wind flow, governing adiabatic energy changes. Inside the TS, $\nabla \cdot V_{sw} > 0$ and adiabatic cooling (energy losses) of CRs occurs. The quantity

$$\Gamma = \frac{E + 2E_0}{E + E_0} \quad (3)$$

is introduced for shorter notation with E being the kinetic energy per nucleon and E_0 the rest mass energy per nucleon (e.g., Jokipii & Kopriva 1979). At present we thus neglect the modulation effects arising from the heliosheath, and the inclusion of these will be left for future study. As pointed out by Florinski & Pogorelov (2009) these effects may well be significant.

We adopt a relatively simple expression for the parallel mean free path $\lambda_{||}$, related to the diffusion coefficient directed parallel to the mean HMF by $\kappa_{||} = v/3\lambda_{||}$, given as

$$\lambda_{||} = \begin{matrix} \lambda_0 (P/P_0)(1 + r/r_0) & \text{if} & P \geq P_0 \\ \lambda_0 (1 + r/r_0) & \text{if} & P < P_0 \end{matrix}. \quad (4)$$

Here, $\lambda_0 = 0.15$ AU, v is the particle speed, $P_0 = 1$ GV, and $r_0 = 1$ AU. This form of $\lambda_{||}$ is not chosen arbitrarily but based on diffusion coefficients used previously in electrons studies (e.g., Potgieter & Ferreira 2002), observations of electron mean free paths near Earth (e.g., Palmer 1982; Dröge 2005), and new advances in diffusion theory (e.g., Teufel & Schlickeiser 2003). More complex expressions for $\lambda_{||}$ (e.g., Engelbrecht & Burger 2010) will be investigated in subsequent work. The essence of the modeling studies in this paper will remain unaffected. We assume isotropic perpendicular diffusion with $\kappa_{\perp\theta} = \kappa_{\perp r} = 0.01\kappa_{||}$ (e.g., Giacalone & Jokipii 1999). Note that, unlike Pei et al. (2010), we do not include a φ dependence in the diffusion coefficients.

For the HMF, the standard Parker (1958) field is assumed, given by

$$B = A_c B_0 \left(\frac{r_0}{r}\right)^2 \left(\mathbf{e}_r - \frac{\Omega r \sin\theta}{V_{sw}}\mathbf{e}_\varphi\right) H(\theta - \theta^t), \quad (5)$$

with B_0 a reference value at r_0, $A_c = \pm 1$ determines the polarity of the HMF, and Ω the angular velocity of the Sun. Here, $B_0 = 5/\sqrt{2}$ nT, $r_0 = 1$ AU, and $A_c = +1$ for the $A > 0$ HMF polarity cycle, leading to $|B| \sim 5$ nT at Earth. The Heaviside step function $H(\theta - \theta^t)$ separates the HMF in hemispheres of opposite polarity, i.e.,

$$H(\theta - \theta^t) = \begin{cases} 1 & \text{if} \quad \theta < \theta^t \\ 0 & \text{if} \quad \theta = \theta^t \\ -1 & \text{if} \quad \theta > \theta^t. \end{cases} \quad (6)$$

Using a flat current sheet for this initial work to separate hemispheres of opposite polarity leads to $\theta^t = \pi/2$. The curvature and gradient of the HMF and its associated heliospheric current sheet (HCS) causes CRs to subsequently undergo gradient, curvature, and HCS drifts. This is quantified in the pitch-angle averaged guiding center drift velocity, given in terms of spherical components as

$$\langle v_d \rangle = v_{dr}\mathbf{e}_r + v_{d\theta}\mathbf{e}_\theta + v_{d\varphi}\mathbf{e}_\varphi. \quad (7)$$

The gradient and curvature components can be calculated directly from the HMF as

$$\langle v_d \rangle^{gc} = Q\frac{P\beta}{3B}\nabla \times \frac{B}{B}, \quad (8)$$

with $Q = \pm 1$ indicating the charge of the CR population, i.e., $Q = -1$ for electrons and $\beta = v/c$ with c being the speed of light (e.g., Jokipii & Kopriva 1979). Drifts in the HCS can be approximated by the expression

$$\langle v_d \rangle^{\text{HCS}} = 0.457 - 0.412\frac{d}{r_L} + 0.0915\frac{d^2}{r_L^2} \cdot A_c Qv(\sin\psi\,\mathbf{e}_r + \cos\psi\,\mathbf{e}_\varphi), \quad (9)$$

with r_L being the Larmor radius, d the distance from the particle's present position (r, θ, φ) to the HCS, $d = |r\cos\theta|$, and $\tan\psi = \Omega r \sin\theta / V_{sw}$ (Burger et al. 1985). The HCS drift velocity is thus directed perpendicular to the HMF and parallel to the HCS itself. Additionally, global CR drifts are believed to be reduced due to the presence of turbulence (scattering; e.g., Minnie et al. 2007). This is incorporated into the modulation model by defining the drift reduction factor as

$$f_s = \frac{(\omega\tau_s)^2}{1 + (\omega\tau_s)^2}, \quad (10)$$

with ω being the particle gyrofrequency and τ_s a scattering timescale. Following Burger et al. (2000) we assume that $\omega\tau_s \approx P/P_0$, and the total drift velocity, as incorporated in the modulation model, becomes

$$\langle v_d \rangle = f_s(\langle v_d \rangle_{gc} + \langle v_d \rangle^{\text{HCS}}) \quad (11)$$

under the required condition that $\nabla \cdot \langle v_d \rangle = 0$.

The Jovian magnetosphere, being the origin of the Jovian electrons, is not handled as a point source, as was mostly done in finite difference models (Ferreira et al. 2001a, 2001b). Indeed, for studies looking at the global modulation of electrons, the volume of the Jovian magnetosphere is negligible compared to that of the heliosphere. In this work, the Jovian magnetosphere is approximated in spherical coordinates as a volume enclosed in a solid angle. The magnetosphere is assumed to be centered at a radial distance of 5.2 AU (in the equatorial plane with varying azimuthal position). The magnetosphere is assumed to be 100 R_J wide in the solar direction (with the Jovian radius $R_J = 71492$ km), 200 R_J in latitudinal and azimuthal extent, and 200 R_J in the tail direction. The modeled intensities are, however, insensitive to the actual volume (size) of the magnetosphere as long as it remains reasonable. Different magnetospheric geometries (e.g., Joy et al. 2002) will be studied in the future.

3. METHOD OF SOLUTION

The set of SDEs derived in the Appendix is solved in a time backward fashion by using the Euler–Maruyama approximation

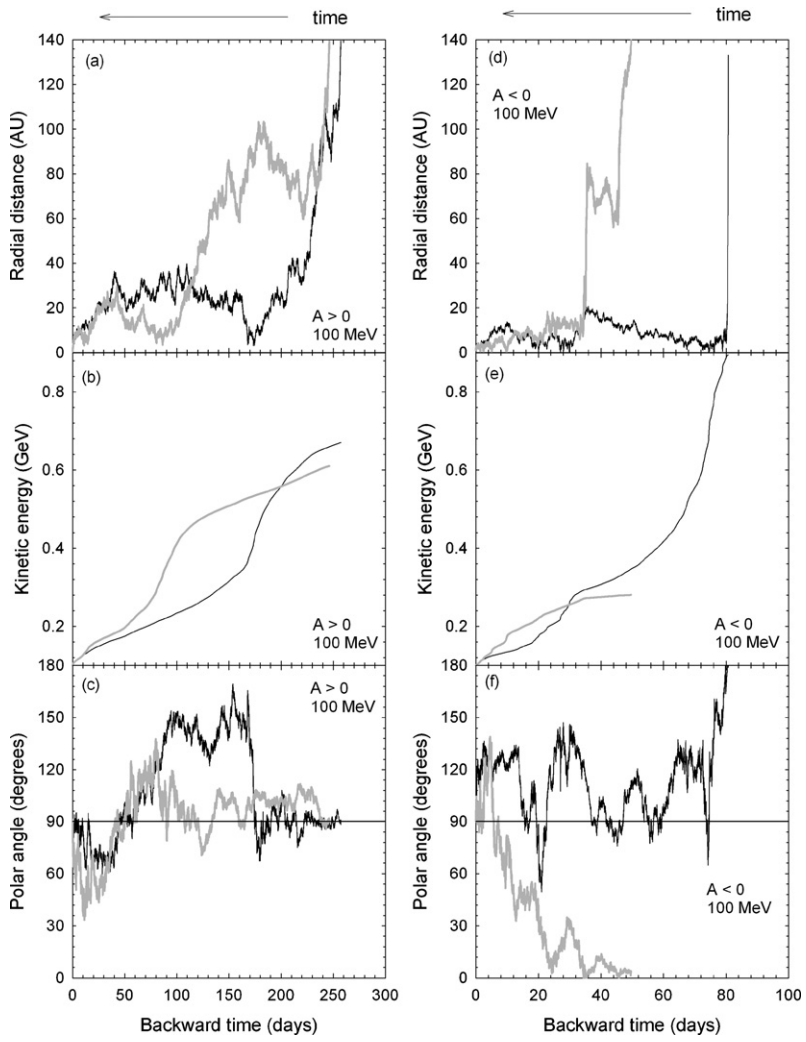

Figure 1. Phase-space trajectories for two pseudo-particles (galactic electrons, black and gray lines) for the $A > 0$ (left panel) and $A < 0$ (right panel) HMF polarity cycles in terms of backward time s. All pseudo-particles trajectories start at $r^0 = 1$ AU, $\theta^0 = \pi$, $\varphi^0 = 0$, $E^0 = 100$ MeV at s^0 and the integration process is continued until the HP is reached.

(Maruyama 1955). This method utilizes the approximation $ds \approx \Delta s$ for the backward time parameter s, ds is the infinitesimal time change, and $\Delta s = 0.004$ days, the time step used in the model. For the different phase-space components, x_i, this gives $dx_i \approx \Delta x_i$ in incremental phase-space steps to describe the evolution of a phase-space density element from an initially specified point (x_i^0, s^0) in an iterative fashion

$$x_i^{j+1}, s^{j+1} = x_i^j, s^j + \Delta x_i^j, \qquad (12)$$

with Δx_i^j evaluated at (x_i^j, s^j), until either an integration boundary or an integration time limit is reached. The resolution of phase space is thus determined by the size of the time increment Δs, with smaller values leading to enhanced integration accuracy, but longer integration times. The numerical error on the calculated intensities can be decomposed as

$$E = E_{\rm sys} + E_{\rm stat} \qquad (13)$$

into systematic and statistical errors. The systematic error depends on the time step $E_{\rm sys} \propto \sqrt{\Delta s}$, while the statistical error

model a further restriction is put on the time step due to the inclusion of the Jovian magnetosphere as a second boundary condition: Δs is chosen such that the resulting average spatial increment is smaller than the size of the Jovian magnetosphere.

For galactic electrons, the outer integration boundary is essentially the heliopause (HP), which we define to be spherical and located at a radial distance of $r_{\rm HP} = 140$ AU. If a solution of j is required, say at Earth, the integration is started at this position (x_i^0, s^0) and iteratively, according to Equation (12), follows the evolution of the phase-space element until the HP is reached where the LIS is specified. Figure 1 shows sample phase-space trajectories in terms of s. These results will be discussed further in Section 4. The phase-space position at which these density elements reach the HP, the so-called *exit position*, is labeled by (x_i^e, s^e). We must integrate over all possible trajectories of these phase-space density elements to successfully complete the integration process. This is simulated by following a large number of these elements up to the integration boundary, and then calculating the differential intensity at the initial position, $j(x^0$ ^{0} $_i, s$), as

$$j \quad _i \qquad 1 \quad ^N$$

i,k k

decreases as the number of traced pseudo-particles increase $E_{\rm stat} \propto 1/N$ (e.g., Kloeden & Platen 1999). For the present

$$= \overline{N}_{k=1} \boldsymbol{j}_{\rm LIS}\ x^e\ , s^e\ , \qquad (14)$$

x^0, s^0

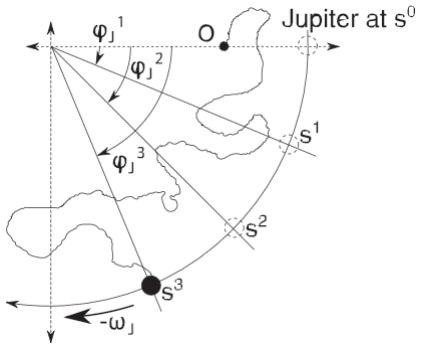

Figure 2. Schematic illustration (not to scale) in the equatorial plane of how the azimuthal position of the Jovian magnetosphere is varied time dependently in the model. At s^0 both the observational point (represented by the small filled circles at O) and the Jovian magnetosphere (represented by the dashed circle) are located at the same azimuthal position, e.g., $\varphi^0 = \varphi_J^0 = 0$. During the integration process, the azimuthal position of the Jovian magnetosphere changes with an angular frequency of $-\omega_J$, while the position of the observation point remains unchanged. The pseudo-particle enters the Jovian magnetosphere at the time s^3 at an azimuthal position φ_J^3, with $\Delta\varphi_J = |\varphi_J^3 - \varphi_J^0|$.

where N is the number of simulated trajectories (i.e., tracing the evolution of phase-space elements) that reach the HP, $\boldsymbol{j}_{\mathrm{LIS}}$ is the LIS, and k refers to the kth density element. The electron LIS of Langner et al. (2001) is used.

It requires some thought to understand what is physically represented by these phase-space trajectories. In essence this is a mathematical realization of the evolution of j throughout the heliosphere. With j both isotropic and gyrotropic, the trajectory of $(x_{i,k}, s_k)$ shows a realization of the evolution of an ensemble (averaged over pitch angle and gyrophase) of particles. As this still remains only a single realization of the particle ensemble, we will refer to these phase-space density elements as *pseudo-particles*. Making this physical connection to the trajectories, we are able to calculate various quantities from the pseudo-particle trajectories, including the so-called *propagation time* (i.e., the time a pseudo-particle spends propagating from its source to an observational point; some authors refer to this as the residence time) as

$$\tau_k = s^e - s^0 \tag{15}$$

$k \quad k$

and thus extract meaningful physical insights from the method of solution itself.

We incorporate the Jovian magnetosphere as a second *boundary condition* and not explicitly as a source, i.e., setting $S = 0$ in Equation (1). This is done by specifying the volume of the magnetosphere V_J. Again starting at (x_i^0, s^0) and tracing the pseudo-particles until $(x_i^e, s^e) \in V_J$, the pseudo-particle is then defined to be of Jovian origin. The intensity of Jovian electrons is then calculated similarly to Equation (14), but substituting $\boldsymbol{j}_{\mathrm{LIS}}$ for the Jovian source function as given by Ferreira et al. (2001b). We also incorporate a time dependence in the position of V_J because of Jupiter's relative position with respect to an observer located at $(r^0, \theta^0, \varphi^0, s^0)$. This is illustrated schematically in Figure 2. The integration process is started at s^0 with the Jovian magnetosphere located at $(r_J, \theta_J, \varphi_J^0)$. The azimuthal position of V_J is then varied as

$$\varphi_J^{j+1} = \varphi_J^j - \omega_J \Delta s, \tag{16}$$

with $\omega_J = 2\pi/4333$ days the orbital angular velocity of Jupiter. A pseudo-Jovian electron will thus encounter Jupiter as a different azimuthal position φ_J^e, after Jupiter has moved a finite distance

$$\Delta\varphi_J = \varphi_J^e - \varphi_J^0. \tag{17}$$

In the next section this effect will be discussed further.

We integrate at least 3000 pseudo-particles for every phase-space position, for both galactic, N_G, and Jovian electrons, N_J. As the fraction of pseudo-particles reaching Jupiter is much less than those reaching the HP (about 1%–10%), we generally have $N_G > N_J > 3000$.

Solving the set of SDEs in spherical coordinates puts further restriction on the integration process, namely, that the spatial coordinates must be re-normalized ("re-set") when moving outside the integration domain. These restrictions are

$$\begin{aligned} \varphi_j < 0 &: \varphi_j \rightarrow \varphi_j + 2\pi \\ \varphi_j > 2\pi &: \varphi_j \rightarrow \varphi_j - 2\pi \\ \theta_j < 0 &: \theta_j \rightarrow |\theta_j|; \varphi_j \rightarrow \varphi_j \pm \pi \\ \theta_j > \pi &: \theta_j \rightarrow 2\pi - \theta_j; \varphi_j \rightarrow \varphi_j \pm \pi. \end{aligned} \tag{18}$$

Although it is computationally expensive to calculate these restrictions at each step of the integration process, it is still computationally much faster than solving the set of SDEs in Cartesian coordinates and transforming back to spherical coordinates at each step.

For the inner boundary, assumed to be the solar source surface, an absorbing boundary condition is used, i.e., pseudo-particles with $r_j < r_\odot = 0.005$ AU are lost to the system. A second choice of boundary condition would be a reflecting boundary condition, i.e., if $r_i < r_\odot \rightarrow r_i = 2r_\odot - r_i$. We however find the resulting solutions insensitive to the assumed boundary condition. As an initial condition, an empty heliosphere is essentially assumed, as discussed in detail by Pei et al. (2010).

In the numerical scheme, integration is continued in time, for each pseudo-particle, until an integration boundary is reached. For this paper, all transport parameters are kept time independent so that CR intensities converge to constant modulation levels in order to compare our results with alternating direction implicit (ADI) steady-state solutions of the TPE (that is, with $\partial f/\partial t = 0$ explicitly in Equation (1)) for solar minimum activity conditions. However, with the introduction of Jovian electrons, the position of the Jovian magnetosphere is changed with time, which is not possible to do with steady-state models, so that the corresponding solutions are time dependent.

3.1. Benchmarking the Modulation Model

We performed various benchmarking procedures in order to validate this modulation approach. Most notable is a comparison with the results of Jokipii & Kopriva (1979), who used a finite difference method to solve the TPE in two dimensions (i.e., in terms of the spatial coordinates r and θ). The reason for choosing their model for benchmarking purposes is that they also used a flat HCS. Figure 3 shows the results for galactic protons in two HMF polarity cycles, with all modulation parameters taken to be the same as given by Jokipii & Kopriva (1979), but with the HCS drift approximated by Equation (9). Zhang (1999) also benchmarked his SDE model with the results of Jokipii & Kopriva (1979) and found similar good agreement. Since his model was solved in Cartesian coordinates, we conclude that our approach, using spherical coordinates, is equally valid and reliable. We thus take the good comparison between the three models as a vindication of the modeling approach used here.

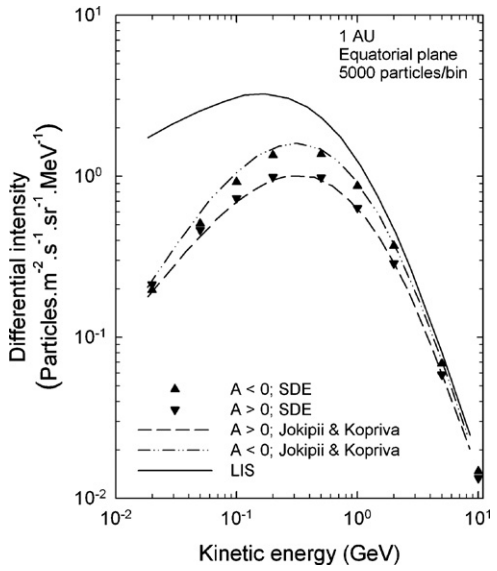

Figure 3. Benchmarking our three-dimensional SDE model with the earlier two-dimensional finite difference model of Jokipii & Kopriva (1979) for the modulation of galactic protons at Earth. Their spectra are shown as lines, with the filled triangles showing our results for the two polarity cycles. The solid line represents the LIS. Here, $N = 5000$ pseudo-particles were traced for each phase-space position in the SDE model.

4. MODELING RESULTS

4.1. Galactic Electrons

Figure 1 shows trajectories for two representative pseudo-particles (gray and black lines) for the $A > 0$ (left panels) and $A < 0$ (right panels) HMF polarity cycles. Here, the phase-space position is shown as a function of backward time *s*, and therefore needs some careful interpretation. Particle simulations start at Earth ($r = 1$ AU, in the equatorial plane $\theta = 90^{\circ}$) and at an energy of 100 MeV. The particle trajectories are then integrated in a time backward fashion until the HP is reached. To interpret the results in the *normal* time forward scenario, one must reverse the process, i.e., starting at the HP and following the trajectories up to Earth. Evidently, CRs undergo diffusive transport from the outer to the inner heliosphere. Note that the trajectories of the spatial coordinates are by no means smooth, but exhibit the stochastic nature of diffusive transport, reflected in the numerical model by the inclusion of the Wiener process (See the Appendix). The energy coordinate (see panels (b) and (e)), on the other hand, is fairly continuous as the evolution of this coordinate is governed by deterministic processes. Following the energy coordinate from the HP until Earth is reached, it is found that for the $A > 0$ polarity cycle, the two electrons entering the heliosphere at an initial energy of $\sim$0.6 GeV undergo adiabatic cooling to reach Earth with an energy of 100 MeV. Lastly, the latitude evolution of the particles shows the general characteristics of drift effects: For the $A > 0$ cycle (panel (c)), the particles stay relatively close to the equatorial plane (where the HCS is located), while for the $A < 0$ cycle the electrons are transported toward the polar regions (panel (f)). This leads to the conclusion that galactic electrons reaching Earth originate mainly from high latitudes in the $A < 0$ cycle, and mainly from low latitudes in the $A > 0$ cycle in qualitative agreement with ADI numerical models. Notable from panel (d) is an apparent jump in the radial position of the simulated particle in the $A < 0$ cycle. Referring to the polar position of this particle (panel (f)), we see that at small radial distances this particle is close to the northern heliospheric pole and due to the geometry of the Parker HMF will have an unphysically high drift velocity (i.e., $v_d \rightarrow \infty$ when $\theta \rightarrow 0, \pi$) and will be transported to the HP *very* quickly. This is the main reason for modifications of the Parker HMF in the polar regions to be implemented, i.e., to avoid the discontinuities directly at the heliospheric poles (e.g., Jokipii & Kóta 1989; Smith & Bieber 1991; Haasbroek & Potgieter 1995).

Switching to Figure 4 we show in the left panel modeled energy spectra at Earth for three cases: a non-drift solution (dotted line), a solution for the $A > 0$ polarity cycle (dashed line), and a solution for the $A < 0$ cycle (dash-dotted line). The solid line shows the assumed unmodulated spectrum (LIS) at the HP. Also included are electron observations at Earth from 1977 ($A > 0$ cycle) and 1965 ($A < 0$ cycle) taken from Potgieter & Moraal (1985) for a qualitative comparison between modeled and observed spectra. This shows that the SDE approach is able to reproduce HMF-polarity-dependent modulation at Earth. Note that below $\sim$30 MeV all computed solutions converge to the non-drift solution, the reason being the drift suppression factor at low energies discussed in the previous section. Again, this is in excellent agreement with ADI modeling of galactic electrons (Potgieter 1996).

The right panel of Figure 4 shows the intensity of 100 MeV galactic electrons as a function of radial distance for both polarity cycles. Because of drift effects, the solutions for different polarity cycles diverge strongly in the inner heliosphere, with the effect subsiding with increasing radial distance to the LIS values as required.

In the top panel of Figure 5, the heliocentric exit position of 100 MeV galactic electrons, traced time backward from Earth, for the $A > 0$ polarity cycle is plotted in terms of their polar and azimuthal angles for 10,000 simulated particles. In this polarity cycle, most of the CRs exit near the equatorial regions. Again interpreting the results in terms of forward time, evidently, the 100 MeV electrons observed at Earth had entered near the equatorial regions. This is again a consequence of general drift considerations. There is no preferred exit position for the azimuthal angle as the Parker HMF has azimuthal symmetry. The polar exit position is binned and shown in the bottom left panel, and once more the preferred exit of CRs in the equatorial regions is clearly seen. Note the logarithmic scaling of the *y*-axis. In the bottom right panel, we bin the exit energy of 100 MeV electrons originally released at Earth. From this follows that most of the simulated particles exit the heliosphere with a final energy of $\sim$0.7 GeV. We thus conclude that (in the time forward case) 100 MeV electrons, observed at Earth, start out at the HP as $\sim$500–1000 MeV electrons which are then adiabatically cooled to 100 MeV.

Figure 6 is similar to Figure 5, but now for the $A < 0$ polarity cycle. In contrast to the $A > 0$ polarity cycle, most galactic electrons in this HMF cycle exit the heliosphere at/near the heliospheric poles. This is again in accordance with the drift consideration in different HMF polarity cycles. An important difference is that the peak of the exit energy now occurs at lower energies, $\sim$500 MeV, than in the $A > 0$ cycle. This is a consequence of the difference in propagation times between the different drift cycles, a fact that will be explored later in this section.

Figure 7 gives a three-dimensional (in terms of spatial coordinates) representation of the same electron trajectories shown in Figure 1. The left panel is for the $A > 0$ cycle, while the right panel is for the $A < 0$ cycle. All axes are labeled in

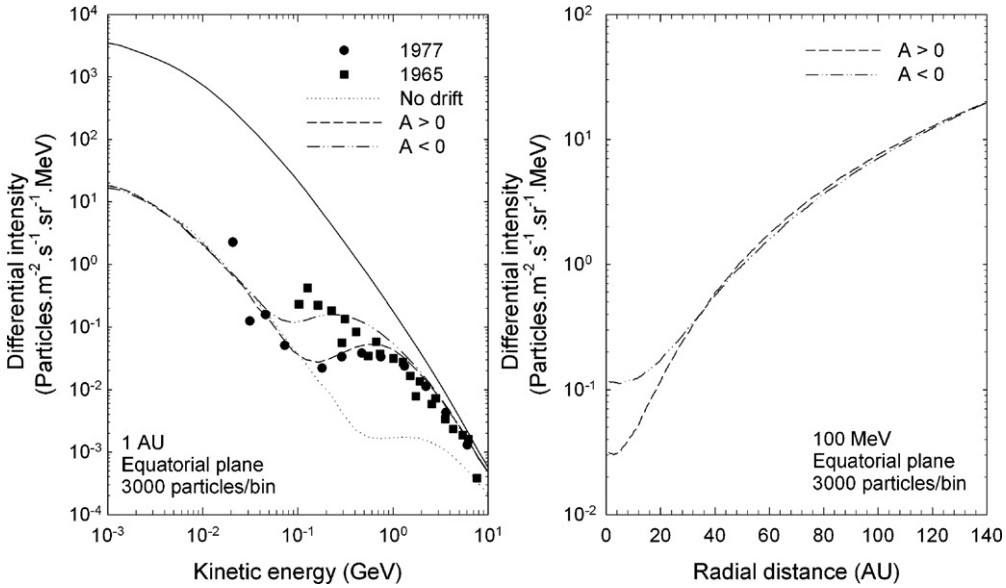

Figure 4. Left panel shows computed galactic electron energy spectra at Earth with respect to the LIS at 140 AU for three cases: neglecting drifts in the model (dotted line), and for the $A > 0$ (dashed lines) and the $A < 0$ (dash-dotted line) HMF polarity cycles. Electron observations at Earth for both HMF cycles ($A < 0$ in 1965 and $A > 0$ in 1977), taken from a compilation by Potgieter & Moraal (1985), are shown for qualitative comparison. The right panel shows computed intensities as a function of radial distance for both polarity cycles at an energy of 100 MeV.

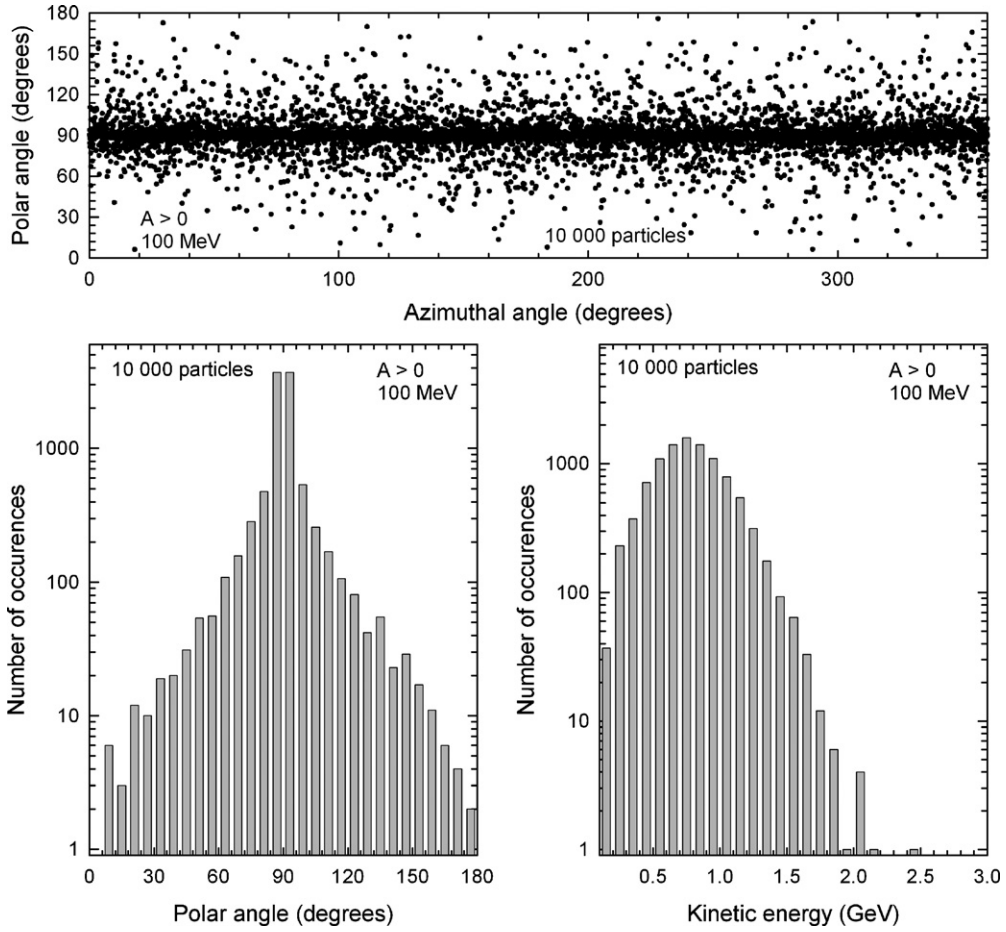

Figure 5. Phase-space exit position at the HP for 10,000 simulated particles (galactic electrons) for the $A > 0$ polarity cycle, initially injected at Earth with an energy of 100 MeV. The top panel shows the exit position in terms of latitude (polar angle) and longitude (azimuthal angle), while the bottom left panel shows the same scenario, but latitude binned. The bottom right panel shows the binned exit energy for galactic electrons originally released at Earth with energies of 100 MeV.

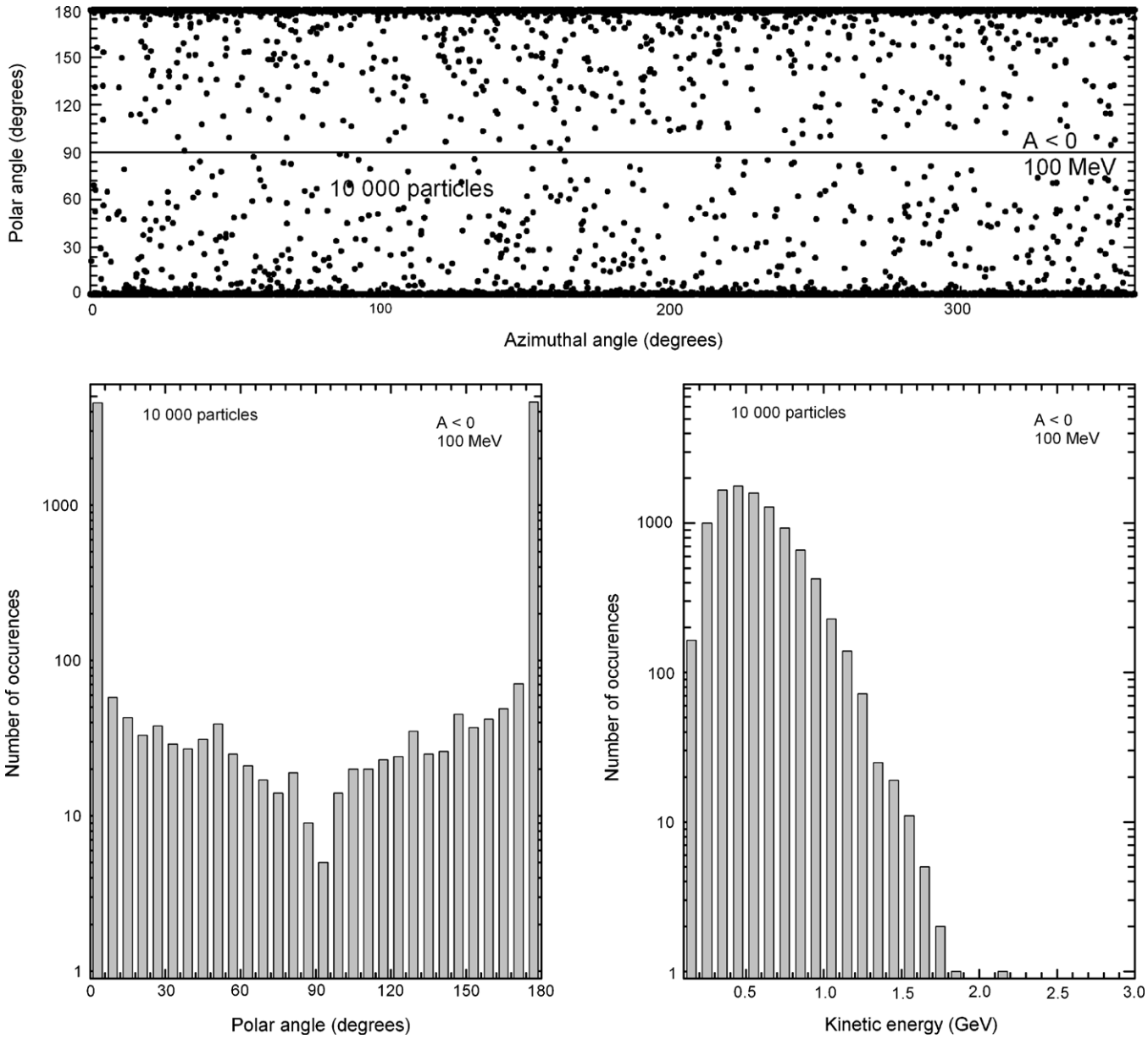

Figure 6. Same as Figure 5, but for the $A < 0$ polarity cycle.

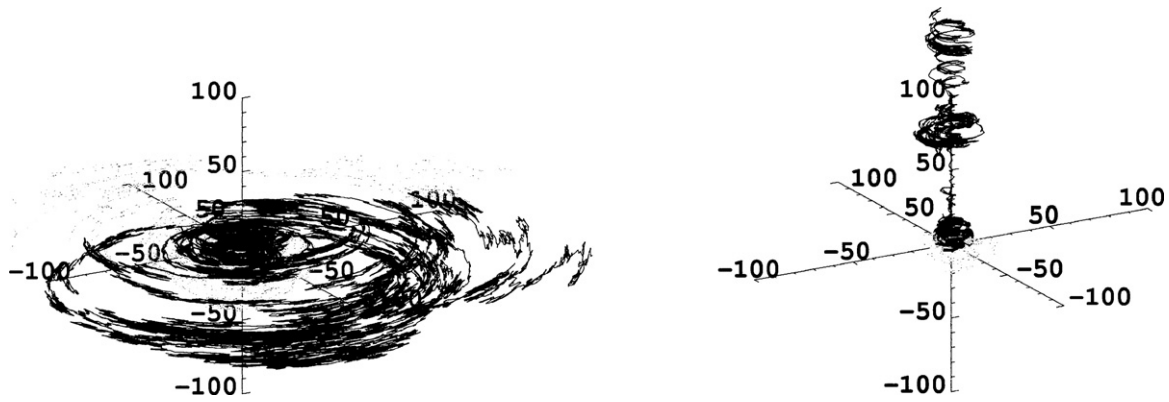

Figure 7. Three-dimensional spatial representation of the particle trajectories shown in Figure 1. Two representative particle trajectories (black and gray lines) are shown for the $A > 0$ (left panel) and $A < 0$ (right panel) HMF polarity cycles. In the $A < 0$ cycle, the pseudo-particles (galactic electrons) are transported mainly toward higher latitudes, while in the $A > 0$ cycle, the particles remain confined to low latitudes and drift outward mainly along the HCS. This illustration is consistent with the results of galactic electrons shown in the previous figure.

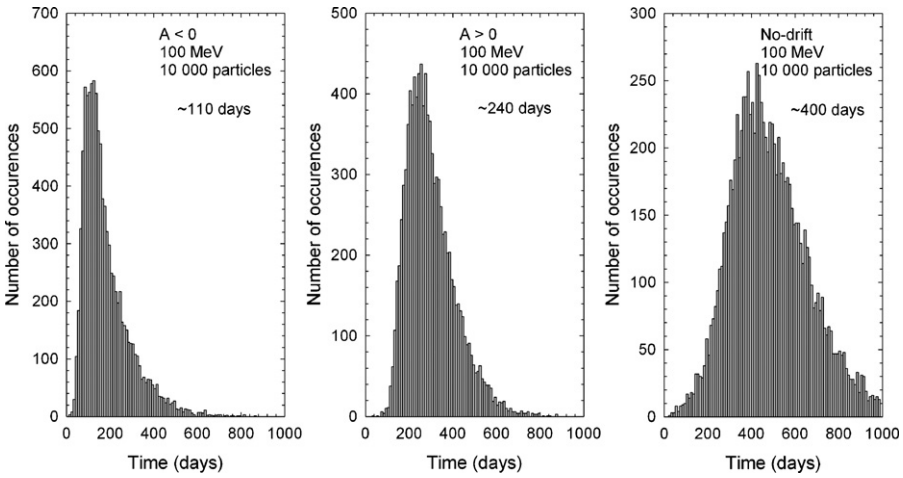

Figure 8. Binned propagation times for galactic electrons released at Earth at 100 MeV for the $A < 0$ (left panel), $A > 0$ (middle panel), and for the no-drift scenarios (right panel). For each computation 10,000 particle trajectories were integrated.

units of AU. This illustration, which is impossible to do with non-SDE models, confirms that electrons observed at Earth during the $A > 0$ cycle drift to the inner heliosphere via the equatorial regions and stay close to the HCS until they reach Earth. For the $A < 0$ cycle, exactly the opposite is seen, where electrons drift from the polar to equatorial regions to reach Earth.

In Figure 8, we show the binned propagation times for galactic electrons initially released at Earth with an energy of 100 MeV. Results are shown for three scenarios: the $A < 0$ polarity cycle (left panel), the $A > 0$ cycle (middle panel), and the non-drift case (right panel). For the latter, the propagation time follows a normal distribution, peaking at ~400 days, while for the different drift cycles, the distribution tends to be more Poisson like (as CR cannot reach the HP infinitely fast, i.e., $\tau > 0$) with lower propagation times. The reason for the shorter propagation times, ~240 days for the $A > 0$ cycle and ~110 days for the $A < 0$ cycle, is that drifts cause a preferred direction of transport for CR electrons, thereby allowing them to escape the heliosphere faster, or in the forward in time case, to propagate faster from the HP to Earth. The propagation times for the $A < 0$ cycle is shorter than for the $A > 0$ cycle, as galactic electrons can more easily escape along the heliospheric poles, but need to drift along the HCS in the $A > 0$ cycle.

To obtain a representative value for the propagation time, we can calculate the expectation value thereof directly from the histogram distribution of τ as

$$\langle \tau \rangle = \sum_{l=1}^{M} \tau_l p_l , \qquad (19)$$

where M is the number of bins and $p_l = N_l/N$ is the probability of finding a particle in a particular bin with propagation time τ_l. Note that $\sum_l p_l = 1$. The expectation value can also be interpreted as the weighted average of the different propagation times. For the $A > 0$ cycle we find $\langle \tau \rangle = 299$ days, for the $A < 0$ cycle $\langle \tau \rangle = 180$ days, and for the non-drift case $\langle \tau \rangle = 481$ days. The expectation values are in general much longer than the peak propagation time due to the long tails in the distribution of τ.

Calculating propagation times allows us to interpret also the energy gain (or loss in terms of forward time) of CR propagating through the heliosphere. The SDE for the energy coordinate leads to $\Delta E \propto \tau$, and CRs with longer propagation times will be more energetic when they reach the HP. The difference in propagation times between the $A > 0$ and $A < 0$ cycles can therefore explain the difference in exit energy shown in Figures 5 and 6. Moreover, the propagation time for the $A > 0$ cycle is a factor of ~2 longer than for the $A < 0$ cycle, and it is generally expected that the electrons in this cycle will undergo more modulation resulting in lower intensities. This is evident from Figure 4: at 100 MeV the electron intensities are much lower for the $A > 0$ cycle. Note that the results given here hold only in the supersonic solar wind where $\nabla \cdot V_{sw} > 0$. It should be noted that the discussion does not include the effect that the rate of energy loss (or gain) depends on the frame in which the CRs are described (Parker 1965; Webb & Gleeson 1979).

4.2. Jovian Electrons

The modeling results shown in this section include both the galactic and Jovian electron populations in the modulation model. The galactic and Jovian electron intensities are calculated simultaneously, but also independently of each other. In the following figures, we therefore show galactic and Jovian intensities separately, as well as the total electron intensity, which is merely a linear combination of the separate components. As previously stated, Jovian electrons dominate the galactic component at low energies and because the effects of drifts are small, even negligible at these low energies, computed intensities are only shown for the $A > 0$ polarity cycle.

Figure 9 shows computed energy spectra, with the inclusion of both galactic and Jovian electrons into the model. The left panel shows the galactic contribution (dashed line), the Jovian contribution (dash-dotted line), and the linear combination of these components (total, solid line) at Earth in the equatorial plane. For these computations, the observer was taken to be located at an azimuthal position of $\varphi^0 = 0$, while Jupiter's position was initially located at $\varphi_J = 0$, but allowed to vary time dependently during the integration process as discussed previously. The right panel is similar, but for an observer located at 5 AU. For both computations, the $A > 0$ cycle is assumed. The results show the same qualitative behavior as discussed previously by Potgieter & Ferreira (2002), with Jovian electrons dominating the combined energy spectrum below ~10 MeV.

In Figure 10 we show the computed total electron intensity as a function of radial distance at an energy of 4 MeV. For all simulations, Jupiter's initial position is kept fixed at $\varphi_J^0 = 0$,

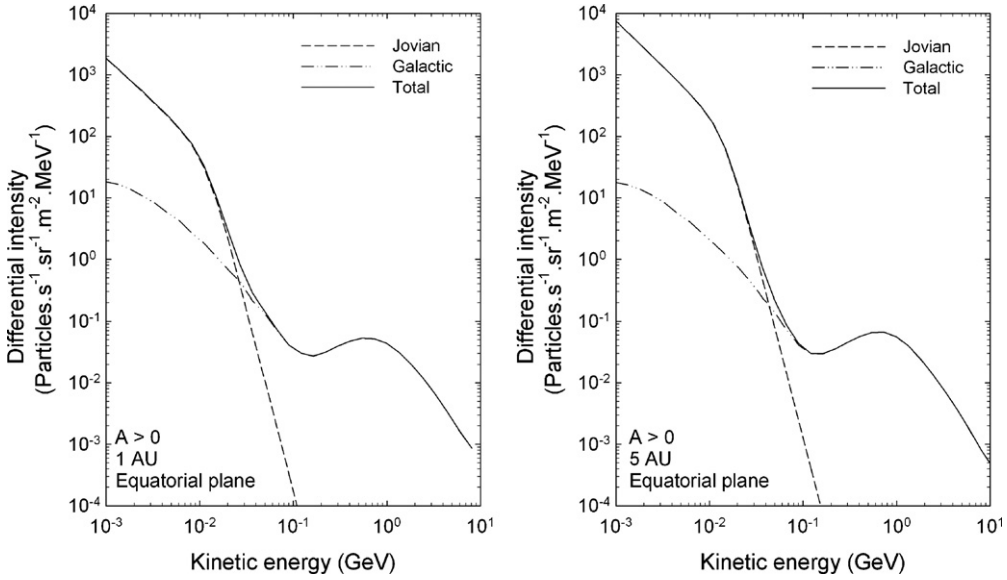

Figure 9. Computed galactic electron (dashed-dotted lines), Jovian electron (dashed lines), and combined electron (i.e., a linear combination of the galactic and Jovian intensities, solid lines) spectra at Earth (left panel) and at 5 AU (right panel) for the $A > 0$ cycle.

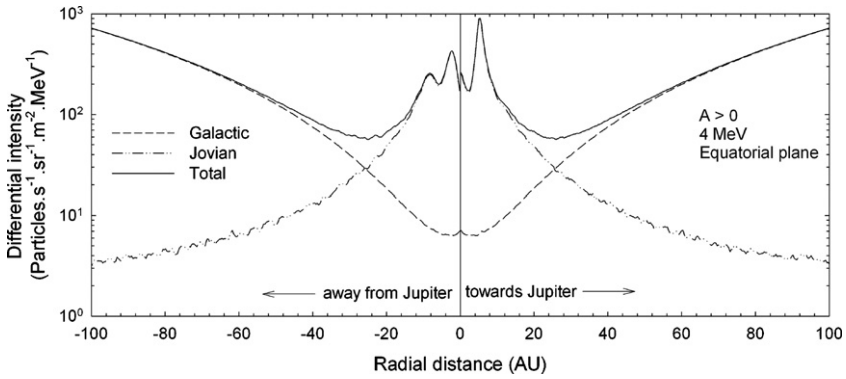

Figure 10. Combined computed galactic and Jovian electron intensities at 4 MeV as a function of radial distance from the Sun, located at the origin. The initial position of the Jovian magnetosphere is kept at $\varphi_J^0 = 0$, while radial cuts at $\varphi = 0$ (toward Jupiter) and $\varphi = \pi$ (away from Jupiter) are shown.

while the right panel shows a radial cut at $\varphi = 0$ (toward Jupiter) and the left at $\varphi = \pi$ (away from Jupiter). From this figure we see that the Jovian electrons dominate the total electron intensity in the inner heliosphere up to ~20 AU in the equatorial plane. This value is however not unique, but depends on the diffusion tensor assumed in the modulation model. In the inner heliosphere, we see four distinctive peaks in electron intensities: the highest one corresponds to the actual position of Jupiter, while the three lower peaks correspond to HMF crossings of field lines connecting the observational point and Jupiter. At $r >$ ~40 AU, the Jovian electron intensities are no longer smooth, but exhibit a wavy behavior. This is caused by the relative motion of Jupiter (discussed next), allowing different field lines to connect the observational point to the Jovian magnetosphere during the integration process.

In the next figure we illustrate the relative motion of the Jovian magnetosphere during the integration process as well as the propagation time of Jovian electrons. The left panel of Figure 11 shows the relative azimuthal motion $\Delta\varphi_J$ of the Jovian magnetosphere when Jovian electrons of 10 MeV are traced time backward from Earth (gray histogram, bottom axis) to the Jovian magnetosphere. This azimuthal motion is due to the finite time a Jovian electron will spend in the heliosphere while propagating from Jupiter to Earth. At these small radial separations between the observational point and the source (i.e., ~5 AU separation between Jupiter and Earth), the relative motion of Jupiter is small, ~1°–2°, during the propagation process and can be neglected as is done in traditional modulation models. At larger radial separations, for an observational point located at 50 AU as an example (black histogram, top axis), the effect of a moving source however becomes larger, ~20°, and contributes to the varying electron intensities shown in Figure 10. The expectation value is $\langle\Delta\varphi_J\rangle = 4^\circ$ for an observational point located at 1 AU, but increases to $\langle\Delta\varphi_J\rangle = 31^\circ$ for an observational point at 50 AU. The propagation times for Jovian electrons, for the same scenarios as in the left panel, are shown in the right panel. None of the Jovian electrons reach Earth in less than 5 days, with the propagation time peaking at ~7 days. These relatively short propagation times make convection and diffusion the effective modulation processes for Jovian electrons in the inner heliosphere, because these particles do not reside long enough in the heliosphere to undergo significant adiabatic energy changes, while drift effects are negligible at these low energies. We find $\langle\tau\rangle = 44$ days at 1 AU and $\langle\tau\rangle = 369$ days at 50 AU.

Next, the geometrical effect of changing the azimuthal separation of Earth (as the observational point) and Jupiter on electron intensities is modeled. The resulting Jovian and galactic intensities are shown in Figure 12. For these simulations the azimuthal

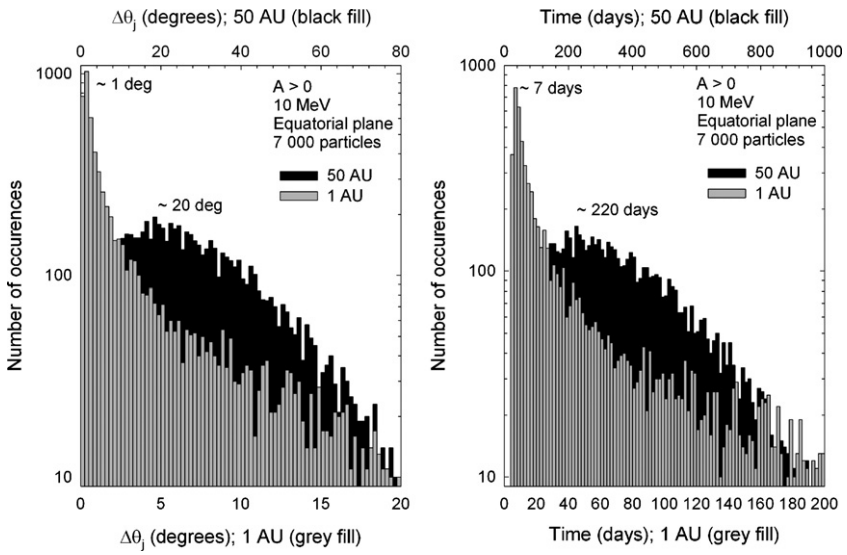

Figure 11. Left panel shows the relative azimuthal motion of Jupiter $\Delta\varphi_J$, when 10 MeV electrons are traced time backward from an observational point at Earth (gray histogram, bottom axis) and from an observational point located at 50 AU in the equatorial plane (black histogram, top axis) from the Jovian magnetosphere. The right panel shows the corresponding propagation times. At Earth, the relative motion of Jupiter is small, $\Delta\varphi_J \sim 1^\circ$, and so is the propagation time of ~7 days. For an observer at 50 AU, however, the relative motion of Jupiter is large $\Delta\varphi_J \sim 20^\circ$, and the propagation time increases to ~220 days.

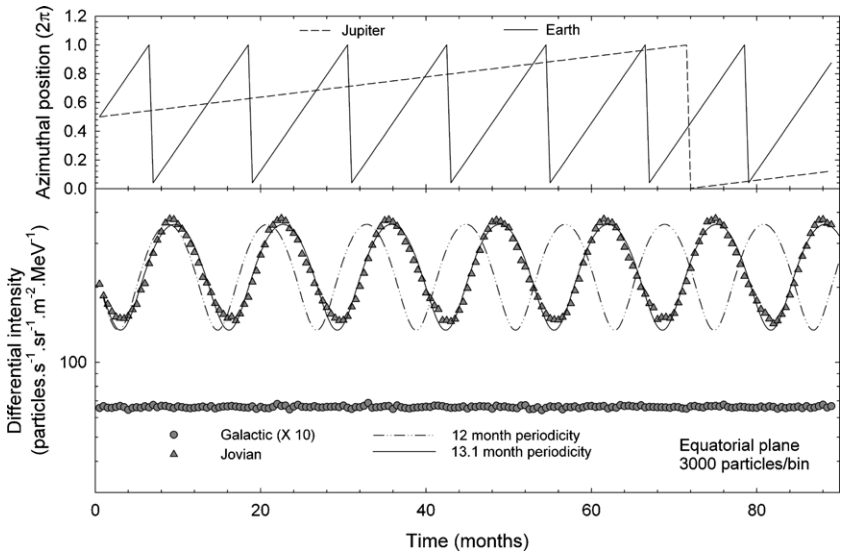

Figure 12. Top panel shows the assumed time-dependent azimuthal positions of Earth and Jupiter in the modulation model, while the bottom panel shows the effect thereof on electron intensities at 4 MeV in the equatorial plane. Jovian intensities are indicated by the triangles and galactic intensities (multiplied by a factor of 10) by the filled circles. The solid and dashed lines show sinusoidal fits to the Jovian intensities, with periods of 13.1 and 12 months, respectively.

position of Earth is varied in accordance with its orbital period of $2\pi/365.25$ day^{-1} and Jupiter with its orbital period of $2\pi/4333$ day^{-1}. Both Earth and Jupiter are initially located at $\varphi = \pi$, as shown in top panel of the figure. In the bottom panel the resulting electron intensities at Earth are shown. For galactic electrons this changing geometry has no effect as the Parker HMF is azimuthally symmetric. For the Jovian electrons, on the other hand, a clear sinusoidal variation with time is found. If the azimuthal position of Jupiter would remain constant over time, a sinusoidal variation with a period of 12 months is expected due to the movement of Earth (shown as the dash-dotted line), but varying the azimuthal separation realistically, we find a period of 13.1 months (solid line). This is in accordance with the observations of, e.g., Moses (1987), and the ADI modeling done previously by Ferreira et al. (2003).

To further emphasize the spatially three-dimensional nature of Jovian electron transport in the inner heliosphere, Figure 13 shows modeled intensity contours in the equatorial (top panel) and meridional (bottom panel) planes at 4 MeV. The position of the Jovian magnetosphere is indicated by the blue asterisk (not to scale), while intensities are normalized to 100% at Jupiter.

5. SUMMARY AND CONCLUSIONS

We discussed a newly developed five-dimensional numerical modulation model applied to the study of galactic and Jovian electrons. Details of the numerical scheme, employing SDEs, were given in Section 3, while a derivation thereof will be given in the Appendix.

Benchmarks for the model were shown in Section 3.1. The model was benchmarked in particular with energy spectra from Jokipii & Kopriva (1979) for galactic protons. Zhang (1999) also benchmarked his five-dimensional SDE model, using Cartesian coordinates, with the same results. We thus find very good comparison with both of these models and take this as a

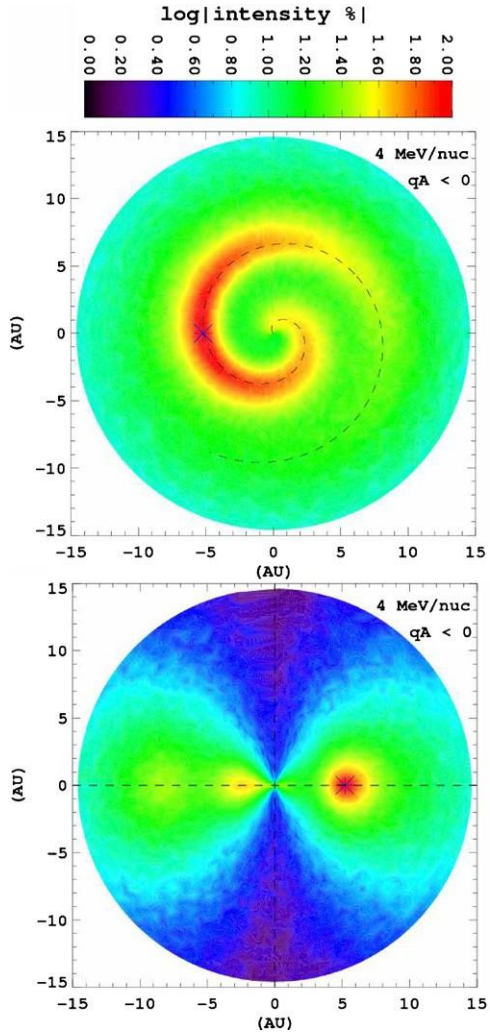

Figure 13. Modeled Jovian electron intensities in the equatorial (top panel) and meridional (bottom panel) planes at 4 MeV. The blue asterisk shows the position of Jupiter, while the dashed line in the top panel shows an HMF line connecting Jupiter to the Sun.

(A color version of this figure is available in the online journal.)

vindication of our SDE modeling approach where the TPE is solved directly in spherical coordinates.

In Figure 4 the resulting energy spectra for galactic electrons were shown for both HMF cycles. A qualitative comparison with observations show that the model can reproduce electron transport in successive drift cycles. Moreover, Figures 5 and 6 show the preferred exit position of galactic electrons in both HMF cycles which are consistent with drift considerations: in the $A > 0$ cycle, most of the CR electrons observed at Earth propagate through the equatorial regions. In contrast, for the $A < 0$ cycle, they reach Earth mainly through the polar regions. This type of study, where the evolution of individual density elements is followed, is not possible with traditional ADI type models.

In Figure 8 the calculated propagation times were shown, again for galactic electrons in both HMF cycles, showing the electrons generally to reside longer in the heliosphere during the $A > 0$ cycle. We find a propagation time of 300 days in the $A > 0$ cycle, 180 days in the $A < 0$ cycle, and 481 days when drifts are completely neglected. We also made the connection between the propagation time and the amount of adiabatic cooling the CR experience. This connection is however only valid in the supersonic solar wind where $\nabla \cdot V_{sw} > 0$ (e.g., Strauss et al. 2010). It is concluded that 100 MeV galactic electrons observed at Earth originate between 500 and 1000 MeV, undergoing adiabatic energy losses during their transport to Earth. Due to the difference in the propagation times between consecutive drift cycles, these electrons undergo additional energy losses in the $A > 0$ cycle due to the their longer propagation time. The ability to calculate the propagation time of CRs is unique to SDE type models.

Energy spectra, as well as radial intensity profiles, with the inclusion of both galactic and Jovian electrons into the modulation model, were shown in Figures 9 and 10. The same qualitative behavior as noted in previous modulation studies was found, with Jovian electrons dominating the galactic contribution at low energies in the inner heliosphere. Notable from Figure 10 is the wavy behavior of the Jovian intensities at large radial distances because of the relative motion of the Jovian magnetosphere included in the present model and shown in Figure 11. For Jovian electrons observed at Earth, the motion of the Jovian magnetosphere, $\sim 4^\circ$, is negligible, while for Jovian electrons reaching 50 AU, this effect can become quite pronounced, $\sim 31^\circ$. In essence, this effect is due to the difference in propagation times between the two scenarios: the mean propagation time between Jupiter and Earth is ~ 44 days, while the propagation time between Jupiter and an observer located at 50 AU is ~ 370 days. Lastly, Figure 12 shows that the model is able to reproduce the well-known ~ 13 month periodicity in Jovian electron intensities as observed at Earth over longer timescales.

It was shown that an SDE-type modulation model can successfully reproduce the modulation of both galactic and Jovian electrons as studied previously by ADI-type models. The method allows us to compute modulation features which are not possible with previous modulation models. This includes calculating the propagation time that CRs spend in the heliosphere and quantifying their energy losses during this period by tracing pseudo-particle trajectories, yielding deeper insight into the modulation process. Because of the numerical stability of the SDE method, we can also include in the model detailed (realistic) descriptions of the heliospheric environment, e.g., including the relative motion of Jupiter.

The authors are grateful for partial financial support provided by the South African National Research Foundation (SANRF) and the Bundesministerium für Bildung and Forschung (BMBF) through the SA-Germany Research Cooperation Program (SUA 08/011) and the Centre for High Performance Computing (CHPC) in South Africa. I.B. acknowledges the "Galactocauses" project (FI 706/9-1), funded by the Deutsche Forschungsgemeinschaft (DFG), and A.K. the "CAWSES" (He 3279/8-3) and He 3279/10-1 projects, funded by the DFG, for partial financial support.

APPENDIX

DERIVING AN APPLICABLE SET OF STOCHASTIC DIFFERENTIAL EQUATIONS FOR COSMIC RAY TRANSPORT

A multidimensional Itō stochastic differential equation (SDE) has the general form

$$dx_i = A_i(x_i)ds + \sum_j B_{ij}(x_i) \cdot dW_i, \qquad \text{(A1)}$$

where $x_i = \{x_i(s), s \geq 0\}$ are Itō processes and s is a time parameter (e.g., Gardiner 1983; Kloeden & Platen 1999; Øksendal 2003). The first term is often referred to as the *drift* term, being continuous and slowly varying, while the second term is called the *diffusion* term and describes a rapidly varying stochastic component. The *drift* term can also be seen as containing deterministic processes, while the *diffusion* term describes random (meaning stochastic of nature) processes via the multidimensional Wiener process $W_i = \{W_i(s), s \geq 0\}$. The Wiener process has a time stationary normal-distributed $N(0, 1)$ probability density with an expectation value of 0 and variance of 1, and can be generated numerically as discussed later. Throughout this work we make use of the index notation $i \in \{r, \theta, \varphi, E\}$ to describe different components of phase space in terms of spherical spatial coordinates and kinetic energy.

Various techniques exist to find the equivalent set of SDEs for a given Fokker–Planck-type equation. In this work we solve the resulting set of SDEs in a time backward fashion and make use of the time backward Kolmogorov equation, given by

$$-\frac{\partial \rho}{\partial s} = \sum_i A_i \frac{\partial \rho}{\partial x_i} + \frac{1}{2} \sum_{i,j} C_{ij} \frac{\partial^2 \rho}{\partial x_i \partial x_j} \,. \tag{A2}$$

Equations (A1) and (A2) are thus equivalent (i.e., describing the same differential equation) to each other by Itō's lemma (Gardiner 1983; Kloeden & Platen 1999). In Equation (A2), $\rho(x_i, s \,|\, x_i^0, s^0)$ is the conditional probability of finding a phase-space density element, with the initial position (x_i^0, s^0), at a position (x_i, s). For Fokker–Planck-type TPEs we can however assume ρ to be proportional to the phase-space density (i.e., distribution function), $\rho \propto \boldsymbol{j}$. Furthermore, we made use of the notation $C_{ij} = (B \cdot B^T)_{ij}$, where T indicates the transpose of the tensor. As we solve the set of SDEs time backward, s is a parameter indicating *backward time*, related to *normal time* t by

$$t = t_N - s, \tag{A3}$$

with t_N being some final time and $s \geq 0$. We thus integrate the set of SDEs from an *initial* time $s = 0, t = t_N$ time backward up to the *present* time $s = t_N, t = 0$. Lastly, we note that $\partial t = -\partial s$, and Equation (A2) becomes

$$\frac{\partial j}{\partial t} = \sum_i A_i \frac{\partial j}{\partial x_i} + \frac{1}{2} \sum_{i,j} C_{ij} \frac{\partial^2 \boldsymbol{j}}{\partial x_i \, \partial x_j} \,. \tag{A4}$$

In essence, this equation thus contains a mixture of time backward phase-space coordinates and forward time (Kloeden & Platen 1999), but allows us to readily obtain the appropriate set of SDEs for CR transport: we rewrite the Parker (1965) TPE in the form of Equation (A4), find the appropriate vector A_i and tensor B_{ij}, and substitute these values into Equation (A1).

Using the assumptions listed in Section (2), the TPE in terms of spherical spatial coordinates and energy becomes

$$\begin{aligned}
\frac{\partial j}{\partial t} = {} & \left[\frac{1}{r^2} \frac{\partial}{\partial r}(r^2 \kappa_{rr}) + \frac{1}{r^2 \sin\theta} \frac{\partial \kappa_{\varphi r}}{\partial \varphi} - V_{\mathrm{sw}} - v_{dr} \right] \frac{\partial j}{\partial r} \\
& + \left[\frac{1}{r^2 \sin\theta} \frac{\partial}{\partial \theta} (\sin\theta \kappa_{\theta\theta}) - \frac{v_{d\theta}}{r} \right] \frac{\partial j}{\partial \theta} \\
& + \left[\frac{1}{\dfrac{r^2}{\sin\theta}} \right] \frac{\partial}{r}
\end{aligned}$$

$$\begin{aligned}
& + \kappa_{rr} \frac{\partial^2 \boldsymbol{j}}{\partial r^2} + \frac{\kappa_{\theta\theta}}{r^2} \frac{\partial^2 \boldsymbol{j}}{\partial \theta^2} + \frac{\kappa_{\varphi\varphi}}{r^2 \sin^2\theta} \frac{\partial^2 \boldsymbol{j}}{\partial \varphi^2} + \frac{2\kappa_{\varphi r}}{r \sin\theta} \frac{\partial^2 \boldsymbol{j}}{\partial r \partial \varphi} \\
& + \frac{1}{3r^2} (r^2 V_{\mathrm{sw}}) \frac{\partial}{\partial E} (\Gamma \boldsymbol{E} \boldsymbol{j}) \,,
\end{aligned} \tag{A5}$$

where the diffusion coefficients, κ_{ij}, are given in terms of spherical coordinates, related to $\mathbf{K}_s$ in HMF coordinates by a rotation about the $\mathbf{e}_\theta$ axis (e.g., Burger et al. 2008). Note that because $\mathbf{K}_s$ is diagonal, the elements $\kappa_{\theta r} = \kappa_{r\theta} = \kappa_{\theta\varphi} = \kappa_{\varphi\theta} = 0$ in terms of spherical coordinates for a Parker HMF configuration. Equation (A5) is already in the form of Equation (A4) with

$$A = [A_r \,, A_\theta \,, A_\varphi \,, A_E \,], \tag{A6}$$

the different components being

$$\begin{aligned}
A_r &= \frac{1}{r^2} \frac{\partial}{\partial r}(r^2 \kappa_{rr}) + \frac{1}{r^2 \sin\theta} \frac{\partial \kappa_{r\varphi}}{\partial \varphi} - V_{\mathrm{sw}} - v_{dr} \,, \\
A_\theta &= \frac{1}{r^2 \sin\theta} \frac{\partial}{\partial \theta} (\sin\theta \kappa_{\theta\theta}) - \frac{v_{d\theta}}{r} \,, \\
A_\varphi &= \frac{1}{r^2 \sin^2\theta} \frac{\kappa_{\varphi\varphi}}{\partial \varphi} + \frac{1}{r^2 \sin\theta} \frac{\partial}{\partial r} \, r\kappa_{r\varphi} \, - \frac{v_{d\varphi}}{r \sin\theta} \,, \\
A_E &= \frac{1}{3r^2} \frac{\partial}{\partial r}(r^2 V_{\mathrm{sw}}) \Gamma E \,,
\end{aligned} \tag{A7}$$

and

$$\mathbf{B}^{\pm} = \pm \sqrt{2} \begin{bmatrix} \sqrt{\kappa_{rr} - \dfrac{\kappa_{\varphi r}^2}{\kappa_{\varphi\varphi}}} & 0 & \dfrac{\kappa_{\varphi r}}{\sqrt{\kappa_{\varphi\varphi}}} \\ 0 & \dfrac{\sqrt{\kappa_{\theta\theta}}}{r} & 0 \\ 0 & 0 & \dfrac{\sqrt{\kappa_{\varphi\varphi}}}{r \sin\theta} \end{bmatrix} . \tag{A8}$$

In Equation (A8) only the spatial elements are taken into account, because the model contains no second-order energy effects at present. Note that the magnitude (and form) of B_{ij} is not uniquely defined due to the presence of off-diagonal terms (e.g., Johnson et al. 2002), but different choices of $\mathbf{B}$ give identical results as they are mathematically equivalent (e.g., Gardiner 1983). Throughout this work we use $\mathbf{B}^+$ from Equation (A8).

Combining all of the results, we have the appropriate set of SDEs to describe the Parker (1965) TPE, given by

$$\begin{aligned}
dr &= \left[\frac{1}{r^2} \frac{\partial}{\partial r}(r^2 \kappa_{rr}) + \frac{1}{r^2 \sin\theta} \frac{\partial \kappa_{r\varphi}}{\partial \varphi} - V_{\mathrm{sw}} - v_{dr} \right] ds \\
&\quad + \sqrt{2\kappa_{rr} - \frac{2\kappa_{r\varphi}^2}{\kappa_{\varphi\varphi}}} \, dW_r + \frac{\sqrt{2\kappa_{r\varphi}}}{\sqrt{\kappa_{\varphi\varphi}}} \, dW_\varphi \\
d\theta &= \left[\frac{1}{r^2 \sin\theta} \frac{\partial}{\partial \theta} (\sin\theta \kappa_{\theta\theta}) - \frac{v_{d\theta}}{r} \right] ds + \frac{\sqrt{2\kappa_{\theta\theta}}}{r} \, dW_\theta \\
d\varphi &= \left[\frac{1}{r^2 \sin^2\theta} \frac{\kappa_{\varphi\varphi}}{\partial \varphi} + \frac{1}{r^2 \sin\theta} \frac{\partial}{\partial r} (r\kappa_{r\varphi}) - \frac{v_{d\varphi}}{r \sin\theta} \right] ds \\
&\quad + \frac{\sqrt{2\kappa_{\varphi\varphi}}}{r \sin\theta} \, dW_\varphi \\
dE &= \frac{1}{3r^2} \frac{\partial}{\partial r}(r^2 V_{\mathrm{sw}}) \Gamma E \, ds
\end{aligned} \tag{A9}$$

for the different phase-space components and backward time s. All transport coefficients are evaluated at the phase-

$\frac{\partial \kappa_{\varphi\varphi}}{\partial \varphi}$ $\frac{v_{d\varphi}}{r \sin\theta}$ $\frac{\partial j}{\partial \varphi}$ space position (x_i, s). Note that this set of SDEs is equivalent to those of Pei et al. (2010).

To simulate independent Wiener processes $W_i(s)$, we make use of the relationship

$$dW_i(s) = \eta(s)\sqrt{ds}, \tag{A10}$$

with $\eta(s)$ a Gaussian distributed (equivalent to a $N(0,1)$ distribution) pseudo-random number (PRN) that can be generated numerically. To simulate the PRNs we implement the well-tested *MT19937* version of the *Mersenne Twister* PRN generating algorithm (Matsumoto & Nishimura 1998) with a proven period of $2^{19937}-1$ to generate standard deviates, i.e., uniformly distributed PRNs on the interval $\mathrm{ffi} \in (0, 1]$ (e.g., Kloeden & Platen
1999), and transform these to Gaussian distributed PRNs by applying the so-called polar method (e.g., Rice 1995), also referred to as the Box–Muller method (e.g., Box & Muller 1958): if $\mathrm{ffi}_1(s)$ and $\mathrm{ffi}_2(s)$ are independent standard deviates, then

$$\eta_1(s) = \sqrt{-2\ln \mathrm{ffi}_1(s)}\cos(2\pi\,\mathrm{ffi}_2(s))$$
$$\eta_2(s) = \sqrt{-2\ln \mathrm{ffi}_1(s)}\sin(2\pi\,\mathrm{ffi}_2(s))$$

are independent Gaussian distributed PRNs. Note that when using the polar method, we have the restriction that $\mathrm{ffi}_{1,2}(s) = 0$.

REFERENCES

Box, G. E. P., & Muller, W. E. 1958, Ann. Math. Stat., 21, 455
Burger, R. A., Krüger, T. P. J., Hitge, M., & Engelbrecht, N. E. 2008, ApJ, 674, 511
Burger, R. A., Moraal, H., & Webb, G. M. 1985, Ap&SS, 116, 107
Burger, R. A., Potgieter, M. S., & Heber, B. 2000, J. Geophys. Res., 105, 27447
Dröge, W. 2005, Adv. Space. Res., 35, 532
Engelbrecht, N. E., & Burger, R. A. 2010, Adv. Space. Res., 45, 1015
Ferreira, S. E. S. 2005, Adv. Space. Res., 35, 586
Ferreira, S. E. S., & Potgieter, M. S. 2002, J. Geophys. Res., 107, 1221
Ferreira, S. E. S., Potgieter, M. S., Burger, R. A., Heber, B., & Fichtner, H. 2001a, J. Geophys. Res., 106, 24979
Ferreira, S. E. S., Potgieter, M. S., Burger, R. A., Heber, B., Fichtner, H., & Lopate, C. 2001b, J. Geophys. Res., 106, 29313
Ferreira, S. E. S., Potgieter, M. S., Heber, B., Fichtner, H., & Wibberenz, G. 2003, J. Geophys. Res., 109, 2115
Fichtner, H., le Roux, J. A., Mall, U., & Rucinski, D. 1996, A&A, 314, 650
Fichtner, H., Potgieter, M. S., Ferreira, S. E. S., & Burger, R. A. 2000, Geophys. Res. Lett., 27, 1611
Florinski, V., & Pogorelov, N. V. 2009, ApJ, 701, 642
Gardiner, C. W. 1983, Handbook of Stochastic Methods (Germany: Springer)
Giacalone, J., & Jokipii, J. R. 1999, ApJ, 520, 204
Haasbroek, L. J., & Potgieter, M. S. 1995, Space Sci. Rev., 72, 385
Heber, B., & Potgieter, M. S. 2006, Space Sci. Rev., 127, 117
Heber, B., & Potgieter, M. S. 2008, in The Heliosphere Through the Solar Activity Cycle, ed. A. Balogh, L. J. Lanzerotti, & S. T. Suess (Germany: Springer-Praxis), 195
Heber, B., et al. 2007, Planet. Space Sci., 55, 1
Johnson, L. W., Reiss, R. D., & Arnold, J. T. 2002, Introduction to Linear Algebra (5th ed.; Reading, MA: Addison-Wesley)
Jokipii, J. R., & Kopriva, D. A. 1979, ApJ, 234, 384
Jokipii, J. R., & Kóta, J. 1989, J. Geophys. Res., 16, 1
Joy, S. P., Kivelson, M. G., Walker, R. J., Khurana, K. K., Russell, C. T., & Ogino, T. 2002, J. Geophys. Res., 107, 1309
Kloeden, P. E., & Platen, E. 1999, Numerical Solution of Stochastic Differential Equations (Germany: Springer)
Krülls, W. M., & Achterberg, A. 1994, A&A, 286, 314
Langner, U. W., de Jager, O. C., & Potgieter, M. S. 2001, Adv. Space. Res., 27, 517
Maruyama, G. 1955, Rend. Circ. Mat. Palermo, 4, 48
Matsumoto, M., & Nishimura, T. 1998, Trans. Model. Comput. Simul., 8, 3
Minnie, J., Bieber, J. W., Matthaeus, W. H., & Burger, R. A. 2007, ApJ, 670, 1149
Moses, D. 1987, ApJ, 313, 471
Øksendal, B. 2003, Stochastic Differential Equations: An Introduction with Applications (Germany: Springer)
Palmer, I. D. 1982, Rev. Geophys. Space Phys., 20, 335
Parker, E. N. 1958, ApJ, 128, 664
Parker, E. N. 1965, Planet. Space Sci., 13, 9
Pei, C., Bieber, J. W., Burger, R. A., & Clem, J. 2010, J. Geophys. Res., 115, A12107
Potgieter, M. S. 1996, J. Geophys. Res., 101, 24411
Potgieter, M. S., & Ferreira, S. E. S. 2002, J. Geophys. Res., 107, 1089
Potgieter, M. S., & Langner, U. W. 2004, ApJ, 602, 993
Potgieter, M. S., & Moraal, H. 1985, ApJ, 294, 425
Rice, J. A. 1995, Mathematical Statistics and Data Analysis (2nd ed.; USA: Duxbury Press)
Smith, C. W., & Bieber, J. W. 1991, ApJ, 370, 435
Strauss, R. D., Potgieter, M. S., Ferreira, S. E. S., & Hill, M. E. 2010, A&A, 522, A35
Teegarden, B. J., McDonald, F. B., Trainor, J. H., Webber, W. R., & Roelof, E. C. 1974, J. Geophys. Res., 79, 3615
Teufel, A., & Schlickeiser, R. 2003, A&A, 397, 15
Webb, G. M., & Gleeson, L. J. 1979, Ap&SS, 30, 335
Yamada, Y., Yanagita, S., & Yoshida, T. 1999, Adv. Space Sci., 23, 505
Zhang, M. 1999, ApJ, 512, 409